Arbitrary power distribution and efficiency optimization for dual-receiver inductive power transfer system with variable coupling

Wenbo Wang, Junjun Deng, Mingyang Li, Mohamed Dahidah, Zhenpo Wang

Abstract-. **In dynamic wireless charging application for electric vehicles, multi-receiver inductive power transfer (IPT) systems hold enormous potential. However, the couplings and the charging rates are significantly different between vehicles and varies randomly, which causes the systems' efficiency deviate from their optimal state. This paper presents an analytical model for solving the optimal control variables, which considers arbitrary loads and couplings. Based on the proposed model, with further considering coupling and load restriction, the feasible regulation trajectories of primary inverter and secondary active rectifier phases are derived. Besides, a maximum efficiency point tracking (MEPT) control strategy are designed for achieving selective power distribution and constant current output characteristics simultaneously. Finally, an IPT experiment with dual loads is designed and carried out. The experimental results show that the ideal power distribution can be maintained for each receiver under load voltage, demand current and coupling variations, furthermore, the efficiency of the proposed system can be improved by 3% to a maximum of 89.13% compared to the system without MEPT.**

Index Terms- **Inductive power transfer, multiple receivers, power distribution, maximum efficiency point tracking.**

I. INTRODUCTION

Inductive Power Transfer (IPT) has made great strides in the last decade and is receiving widely increased attention in both industry and academia[1]. By transferring energy from the transmitter (TX) to the receiver (RX) via electromagnetic fields without the need for electrical contact, IPT offers the advantages of safety, convenience and flexibility. Due to its superior characteristics, it has been successfully applied in medical devices[2], consumer electronics[3], drones[4], wireless motors[5], wireless lighting[6], electric vehicles [7-8]and so on.

Charging multiple RXs at the same time using one TX is another unique advantage of IPT systems and, with the development of IPT technology, the demand for single-TX coupled with multiple-RXs (TX-RXs) IPT systems is growing rapidly[9-10]. In this regard, the need for differentiated IPT output is increasingly prominent, as devices in the TX-RXs IPT system often operate with different load characteristics and power levels. For example, to W-class consumer electronics, the charging board needs to cover devices such as mobile phones, computers and watches, whereas there are variations in the power consumption of individual appliances that require different charging power allocations[11]. For kW-class electric vehicles (EV), a section of the charging coil can simultaneously charge multiple vehicles as shown in Fig. 1, which has potential for applications in static charging[12,13], semi-dynamic charging at intersections[14, 15], and dynamic charging[16]. While using IPT to charge EVs, there are two key points to consider: 1) Due to driving or parking tolerances, the coupling of each vehicle may vary, which impacts the stability of the charging power[17,18,19] 2) As the battery and charging requirements of vehicles are differentiated, it is essential that the system can satisfy power distribution requirements[20,21]. Therefore, for the purpose of improving the power stability and suitability of the TX-RXs system in EVs charging scenarios, the coupling variation and power distribution should to be considered simultaneously.

In order to achieve differentiated output requirements, abundant research have been carried out, focusing on couplers, compensation topology and control strategies. A comparative study of the power transfer characteristics between coupled coils is carried out by[22], revealing the principle of magnetic field transfer between rectangular coils and DD coils, whereby the differentiated output of the system can be achieved by combining coils of different configurations[23]. In terms of compensation topology, the main objective is to achieve load-independent output and non-interference of the individual RXs outputs. SS topology provides a load-independent constant current output in single TX to single RX scenario, but it fails to decouple the current between individual loads in multi RXs application, mainly due to the fact that for SS topology the current in the TX coil is subject to load variations[24]. In
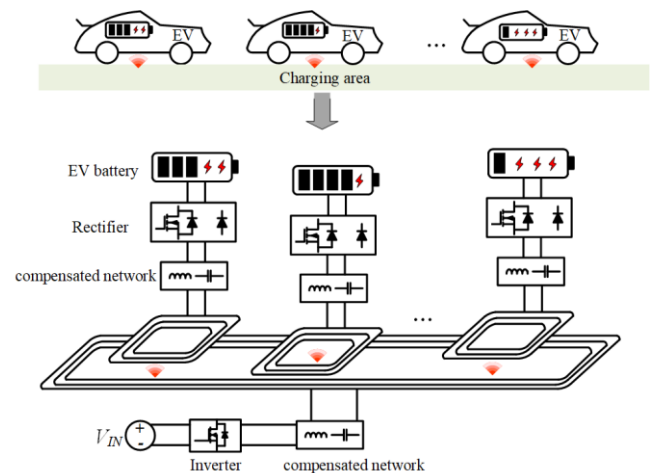

Fig. 1. Application of IPT system to charge multiple EVs.

contrast, the LCC topology is known for its clamped TX coil currents, moreover, the LCC-LCC compensation network with both sides LCC not only guarantees load-independent rectifier input currents, but also provides a higher degree of design freedom, making it suitable for TX-RXs applications[25].

A well-performing IPT system not only relies on an excellent passive circuit design, but also depends on the control strategy to meet the power distribution requirements. In this regards, multi-frequency modulation, time-division multiplexing and impedance matching are mainly adapted to realize the power distribution of RXs. By setting different resonant frequencies for the RXs, power distribution can be achieved by selectively transferring power to the target load through frequency regulation[26,27]. However, in the case of multi-frequency modulation, the impedances between multiple RXs may interact with each other. This undesirable phenomena can be severe, leading to uncontrollable power distribution [10]. Time-division multiplexing, on the other hand, refers to splitting the power supply to different loads over several times, thus allowing the system to be simplified to a single-to-single control system. Optimal efficiency and power distribution can then be achieved using single-to-single control strategy[28], but time-division multiplexing increases the power transmission delay and requires additional control circuitry to select the operational RX[29]. In addition, the power distribution between RXs can be effectively adjusted by impedance matching, specifically by adding DC-DC converters[30] or capacitor arrays[31], obviously, adding additional components increases the circuit complexity and cause large volume. Similarly, in [32] power distribution and efficiency optimization are simultaneously achieved by cascade DC-DC converter both in transmitter and receivers. However, it still increases complexity and size in receiver which is not attractive in EV charging, an optimal control scheme should take proper account of the available system components. In contrast, the use of controlled rectifier for impedance matching and power distribution is a more attractive choice. The power distribution between the individual loads has been achieved by modifying the rectifier at the RXs side[33,34]. Besides, by replacing the uncontrolled rectifier on the receiver with an active bridge, the power distribution can also be achieved[35]. However, the aforementioned works neglect the coupling and load voltage differences, and ignoring these differences can lead to misallocation in power distribution.

Furthermore, in the case of the TX-RXs charging environment, the MEPT method is essential to improve the efficiency of the overall system. The basic principle of the regulation methods is to optimize the current in the resonant cavity by adjusting the control parameters, therefore to attenuate the losses in the system[36-39]. Accordingly, MEPT is usually implemented in TX-RXs systems by setting the optimum load value[40], adjusting the system operating frequency[26] and regulating the system input voltage[41]. However, currently implemented MEPTs are mainly focus on specific coupling or identical load states, whereas in real scenarios such as EVs charging the coupling and load of RXs

tend to vary randomly, hence it is necessary to carry out further analysis and research on MEPTs for multiple RXs systems.

Briefly, in TX-RXs systems with varying charging requirements and different coupling states, there is an urgent need to address the issues of selective power allocation, load-independent output characteristics and MEPT. The scenario for this paper is derived from a mini-EV project which required the supply of power to two separate loads with varying output characteristics. Firstly, a modular equivalent circuit for a TX to dual RXs is derived and output characteristics of the circuit are analyzed, followed by a system loss model revealing the correlation between AC input voltage and maximum efficiency. Finally, a detailed experimental test of the MEPT method is carried out, the main contributions of this paper are summarized as follows.

1) For multi-RX IPT systems, an analysis model based on dual active bridge is presented, which can realize differentiated constant current output and efficiency optimization simultaneously under varying loads and coupling.

2) Based on the proposed model, the transmitter regulation trajectory for maximizing system efficiency is further addressed by considering the coupling of AC input voltages and load state constraints. Moreover, a dual-side charging MEPT strategy based on the perturbation observation method is introduced, where the phase of the active rectifier is adjusted independently to achieve output regulation, and the phase of the inverter is adjusted with the objective of minimizing the input DC current to achieve MEPT.

The remainder of this paper is organized as follows. System modelling and analysis is developed in Section II, whereas the analysis of the MEPT method is discussed in Section III. Section IV develops the model and verifies the feasibility of the theoretical analysis. Finally, Section V concludes the paper.

II. THEORETICAL ANALYSIS

A. System structure

The LCC-LCC compensated IPT system with active rectifiers is shown in Fig. 2. Due to the need to maintain a
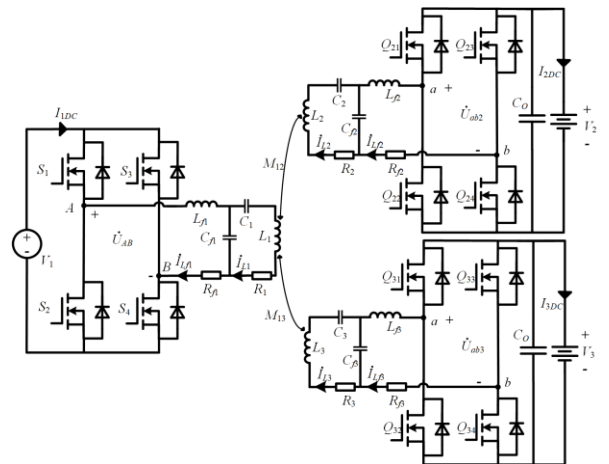

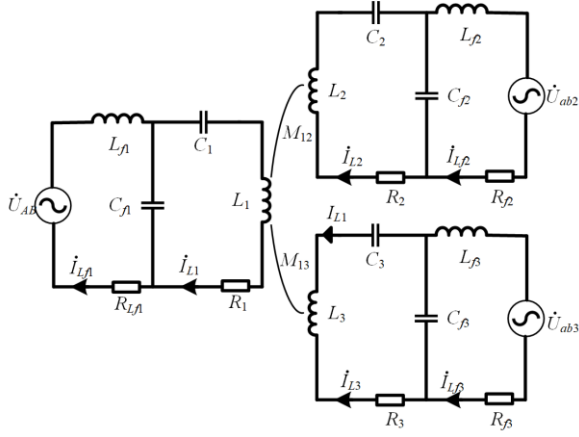Fig. 2. Schematic diagram of a dynamic system with dual receivers employing an LCC-LCC compensation

Fig 3. Equivalent circuit of a dynamic system with dual RXs employing an LCC-LCC compensation

safety distance between vehicles, there is no cross-coupling between the two RXs. On the transmitter side, V_1 is the DC input voltage, and a full bridge consist of MOSFETs S_1-S_4 is used to generate AC input voltage. An LCC compensation network consists of L_{f1}, C_{f1}, C_1 are adopt to generate a constant current in the transmitter coil L_1. On the receiver side, V_2 and V_3 represent the dc output voltage, the structure of the two RXs is identical, with the same LCC compensation networks (L_{f2}, C_{f2}, C_2, L_{f3}, C_{f3}, C_3) and controlled rectifier (Q_{21}-Q_{24}, Q_{31}-Q_{34}). However, the two RXs are completely decoupled, with independent charging current requirements (I_{2DC}, I_{3DC}) and different mutual inductance (M_{12}, M_{13}). Moreover, R_1, R_2, R_3 indicate the Equivalent Series Resistances (ESRs) of each loop, R_{f1}, R_{f2}, R_{f3} represents the sum of the equivalent series resistance (ESR) of each circuit and the on-resistance of the two MOSFETs.

For ease of analysis, the fundamental harmonic approximation is used because of its sufficient accuracy where all the higher harmonics are negligible. The simplified equivalent circuit is shown in Fig. 3, where U_{AB}, U_{ab2} and U_{ab3}
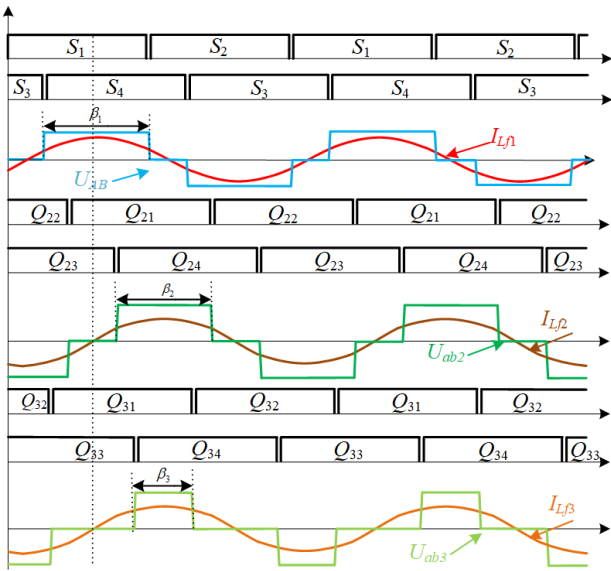

Fig 4. Key-waveforms of the inverter and active rectifiers

represent the RMS values of $\dot{U}_{AB}$, $\dot{U}_{ab2}$ and $\dot{U}_{ab3}$, and the current is represented in a similar way.

B. Circuit analysis of the resonant network

To ensure the system works at a resonance mode, the component parameters of the LCC-LCC compensation network should satisfy the following principles:

$$\omega^2 L_{f1} C_{f1} = 1, \omega^2 (L_1 - L_{f1}) C_{f1} = 1$$
$$\omega^2 L_{f2} C_{f2} = 1, \omega^2 (L_2 - L_{f2}) C_{f2} = 1 \quad (1)$$
$$\omega^2 L_{f3} C_{f3} = 1, \omega^2 (L_3 - L_{f3}) C_{f3} = 1$$

On the basis of Kirchhoff's voltage law (KVL) and superposition theory applied in [42], while ignoring the system's ESRs, the single-to-dual LCC-LCC compensation topology can be mathematically described as

$$
\begin{bmatrix}
0 & j\omega L_{f1} & 0 & 0 & 0 & 0 \\
j\omega L_{f1} & 0 & 0 & j\omega M_{12} & 0 & j\omega M_{12} \\
1 & 0 & \dfrac{j\omega L_{f1} L_{f1}}{M_{12}} & 0 & 0 & 0 \\
0 & 0 & 0 & j\omega L_{f2} & 0 & 0 \\
1 & 0 & 0 & 0 & \dfrac{j\omega L_{f1} L_{f3}}{M_{12}} & 0 \\
0 & 0 & 0 & 0 & 0 & j\omega L_{f3}
\end{bmatrix}
\begin{bmatrix}
\dot{I}_{Lf1} \\ \dot{I}_{L1} \\ \dot{I}_{Lf2} \\ \dot{I}_{L2} \\ \dot{I}_{Lf3} \\ \dot{I}_{L3}
\end{bmatrix}
=
\begin{bmatrix}
\dot{U}_{AB} \\ 0 \\ 0 \\ \dot{U}_{ab2} \\ 0 \\ \dot{U}_{ab3}
\end{bmatrix}
\quad (2)
$$

where, $\omega = 2\pi f$ is the angular frequency of the system. According to (2), the current in each loop can be derived as

$$\dot{I}_{Lf1} = \frac{M_{12} \dot{U}_{ab2}}{\omega L_{f1} L_{f2}} + \frac{M_{13} \dot{U}_{ab3}}{\omega L_{f1} L_{f3}}, \dot{I}_{L1} = \frac{\dot{U}_{AB}}{j\omega L_{f1}}$$

$$\dot{I}_{Lf2} = \frac{M_{12} \dot{U}_{AB}}{\omega L_{f1} L_{f2}}, \dot{I}_{L2} = \frac{\dot{U}_{ab2}}{\omega L_{f2}}, \dot{I}_{Lf3} = \frac{M_{13} \dot{U}_{AB}}{\omega L_{f1} L_{f3}}, \dot{I}_{L3} = \frac{\dot{U}_{ab3}}{\omega L_{f3}}$$

(3)

Since $\dot{U}_{ab2}$ and $\dot{U}_{ab3}$ are passive voltages generated by the active rectifier, $\dot{U}_{ab2}$ and $\dot{U}_{ab3}$ should in phase with $\dot{I}_{Lf2}$ and $\dot{I}_{Lf3}$. Therefore, the output power of the system can be obtained as

$$P_{out} = \dot{I}_{Lf2} \dot{U}_{ab2} + \dot{I}_{Lf3} \dot{U}_{ab3} = \frac{M_{12} U_{AB} U_{ab2}}{\omega L_{f1} L_{f2}} + \frac{M_{13} U_{AB} U_{ab3}}{\omega L_{f1} L_{f3}} \quad (4)$$

Considering the power loss caused by ESRs in each loop, the efficiency of the system can be derived as

$$\eta = \frac{P_{out}}{P_{Rfi} + P_{Ri} + P_{out}} (i = 1, 2, 3)$$

(5)

$$P_{Rfi} = \sum_{i=1}^{3} I_{Lfi}^2 R_{Lfi}, P_{Ri} = \sum_{i=1}^{3} I_{Li}^2 R_i$$

The coupling and AC voltage of both RXs are independent of each other and can be represented by

$$\frac{U_{ab2}}{U_{ab3}} = \sigma, \frac{M_{12}}{M_{13}} = \varepsilon \quad (6)$$

It can be assumed that both RXs have the same length of wire for the inductor and compensating inductor and therefore can be treated as having the same internal resistance in their circuits, as follows

$$R_2 = R_3, R_{f2} = R_{f3} \quad (7)$$

By combining (3), (5), (6) and (7), the system efficiency can be simplified as

$$\eta_0 = 1/(AU_{AB} + \frac{B}{U_{AB}} + 1) \qquad (8)$$

$$A = \frac{\sigma(\varepsilon^2(R_{L1}L_{f2}^2 + R_{Lf2}M_{12}^2) + R_{Lf2}M_{12}^2)}{\omega M_{12}L_{f1}L_{f2}\varepsilon(\sigma\varepsilon + 1)U_{ab,2}}$$

$$B = U_{ab2}\frac{((L_{f1}^2R_{L2} + R_{Lf1}M_{12}^2)\sigma^2 + L_{f1}^2R_{L2})\varepsilon^2 + (2\sigma\varepsilon + 1)R_{Lf1}M_{12}^2}{\omega M_{12}^2 L_{f1}L_{f2}\sigma\varepsilon(\sigma\varepsilon + 1)}$$

As evident from (8), when U_{ab2} is independent of U_{AB}, then the system efficiency is dependent on the input voltage U_{AB} and there is an optimal voltage value that maximizes the system efficiency. By setting the derivative of η with respect to U_{AB} to zero, the optimal input AC voltage U_{AB} can be obtained as

$$U_{AB-opt0} = (B/A)^{1/2} =$$

$$U_{ab2}\sqrt{\frac{((L_{f1}^2R_{L2} + R_{Lf1}M_{12}^2)\sigma^2 + L_{f1}^2R_{L2})\varepsilon^2 + (2\sigma\varepsilon + 1)R_{Lf1}M_{12}^2}{\sigma^2(\varepsilon^2(R_{L1}L_{f2}^2 + R_{Lf2}M_{12}^2) + R_{Lf2}M_{12}^2)}} \qquad (9)$$

C. Efficiency optimization with controlled rectifiers

In this paper, controlled rectifiers are used for output regulation due to the effective reduction in system volum. Fig. 4 illustrates the main waveforms of the IPT system with controlled rectifiers applied at the receiver side. Here, the Phase Shift (PS) modulation method is used to regulate the output current (I_{2DC}, I_{3DC}), and the DC current and voltage of the rectifiers can be expressed as

$$I_{2DC} = \frac{2\sqrt{2}}{\pi}I_{Lf2}\sin(\beta_2), V_2 = \frac{\pi}{2\sqrt{2}}\frac{U_{ab2}}{\sin(\beta_2)}$$

$$I_{3DC} = \frac{2\sqrt{2}}{\pi}I_{Lf3}\sin(\beta_3), V_3 = \frac{\pi}{2\sqrt{2}}\frac{U_{ab3}}{\sin(\beta_3)} \qquad (10)$$

By combining (10) and (4), the AC voltage at the two RXs can be obtained as

$$U_{ab2} = \frac{V_2\omega L_{f1}L_{f2}I_{2DC}}{M_{12}U_{AB}}, U_{ab3} = \frac{V_3\omega L_{f1}L_{f3}I_{3DC}}{M_{13}U_{AB}} \qquad (11)$$

It should be noted that U_{ab2} is correlated with U_{AB} when a active rectifier is used to control the output, so solving for the efficiency would require reformulating (5). Assuming that the ratio of the battery voltage and current requirement at the RX side is

Symb	Val	Symb	Val	Symb	Val
f	85kHz	C_{f1}	116.16 nF	R_1	1000mΩ
L_1	230μH	C_{f2}	232.33 nF	R_{L2}	360mΩ
L_2	106μH	C_{f3}	232.33 nF	R_{L3}	360mΩ
L_3	106μH	U_{AB}	100-180 V	R_{f1}	102mΩ
L_{f1}	30.18μH	V_2	80-120 V	R_{f2}	72mΩ
L_{f2}	15.09μH	V_3	80-120 V	R_{f3}	72mΩ
L_{f3}	15.09μH	M_{12}	14-28 μH	α	0.67-1.5
C_1	17.54nF	M_{13}	14-28 μH	γ	0.45-2.2
C_2	38.56 nF	I_{2DC}	5-11 A	ε	0.5-2
C_3	38.56 nF	I_{3DC}	5-11 A		

$$\frac{V_2}{V_3} = \alpha, \frac{I_{2DC}}{I_{3DC}} = \gamma \qquad (12)$$

Incorporating (11) with (12), the AC voltage relationship between the two RXs can be rewritten as

$$\frac{U_{ab2}}{U_{ab3}} = \frac{\alpha \cdot \gamma}{\varepsilon} \qquad (13)$$

By combining (3), (5), (6), and (13), the system efficiency can be further simplified as

$$\eta = 1/(XU_{AB}^2 + \frac{Y}{U_{AB}^2} + 1) \qquad (14)$$

$$X = \frac{(\alpha^2\lambda^2\varepsilon^2(R_{L1}M_{12}^2L_{f2}^2 + R_{Lf2}M_{12}^4) + R_{Lf2}M_{12}^4\alpha^2\lambda^2)}{\omega^2 M_{12}^2 L_{f1}^2 L_{f2}^2\alpha\lambda\varepsilon^2(\alpha\lambda + 1)V_2 I_{2DC}}$$

$$Y = \frac{(R_{Lf1}M_{12}^2(\alpha\lambda + 1)^2 + L_{f1}^2R_{L2}(\alpha^2\lambda^2 + \varepsilon^2))V_2 I_{2DC}}{M_{12}^2\alpha\lambda(\alpha\lambda + 1)U_{AB}^2}$$

By setting the derivative of η with respect to U_{AB}^2 to zero, the optimal input AC voltage U_{AB} can be derived as

$$U_{AB-opt} = (Y/X)^{1/4}$$

$$= (\frac{(R_{Lf1}M_{12}^2(\alpha\lambda + 1)^2 + L_{f1}^2R_{L2}(\alpha^2\lambda^2 + \varepsilon^2))}{\alpha^2\lambda^2 M_{12}^2(R_{Lf2}M_{12}^2(\varepsilon^2 + 1) + \varepsilon^2 R_{L1}L_{f2}^2)}$$

$$\cdot \varepsilon^2\omega^2 L_{f1}^2 L_{f2}^2 V_2^2 I_{2DC}^2)^{1/4} \qquad (15)$$

In order to make the above analysis more intuitive, an example of single-to-dual system is designed based on the compensation relation of (10) with parameters tabulated in Table I. The efficiency of the system for different output voltage ratios α, output current ratios γ and mutual inductance
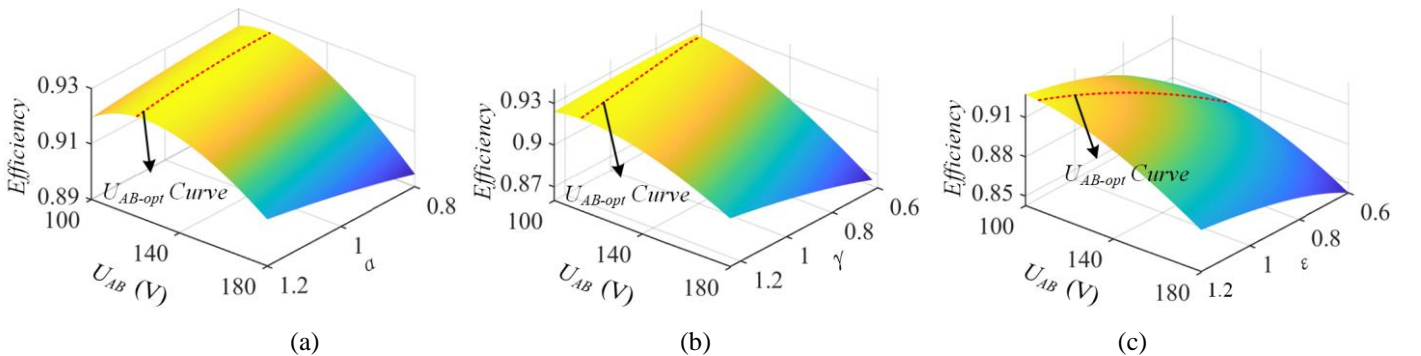

Fig 5. The trend surface of the efficiency with U_{AB} and α, γ and ε (a) U_{AB} with α (V_3=100V,I_{3DC}=10A, M_{13}=28μH, γ=1 and ε=1); (b) U_{AB} with γ (V_3=90V,I_{3DC} =9A, M_{13}=28μH, α=1 and ε=1); (c) U_{AB} with ε (V_3=80V,I_{3DC} =8A, M_{13}=23.3μH, α=1.1 and γ=0.9).
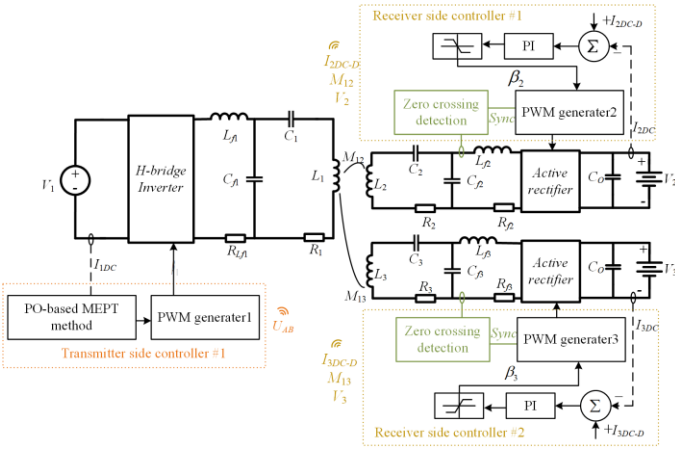
Fig 6. Close loop control diagram.

ratio ε with different input voltages U_{AB} is shown in Fig. 5.

It can be clearly observed that the change of input voltage has a significant effect on the system efficiency, which is a convex function of the input voltage as described by (14). Therefore, there is a corresponding optimal input voltage for various α, γ as well as ε, where the system efficiency can be maximized.

III. The PROPOSED MEPT METHOD WITH DUAL-SIDE CONTROL

In this section, the dual side control scheme of the proposed MEPT method is analyzed in detail. A closed loop control diagram is depicted in Fig. 6. On the TX side, a maximum efficiency point is tracked by measuring the system input DC current using a perturbation observation (PO) algorithm. On the RX side, the conduction angles (β_2, β_3) of the active rectifiers are altered according to the different charging current requirements.

A. Receiver side control for required output

The main control goal is to provide the required power according to the charging state of the vehicle battery. Meanwhile, the output current demand (I_{2DC-D}, I_{3DC-D}), battery voltage (V_2, V_3) and mutual inductance (M_{12}, M_{13}) should all be fed back via Bluetooth to the transmitter side to calculate the optimum U_{AB}. In addition, the communication rates required for the above three signals in the control loop are not of primary concern, as the battery voltage, current demand and mutual inductance during charging do not suffer from drastic variations.

The phases of I_{Lf2} and I_{Lf3} are captured by zero crossing detection. With the assistance of zero crossing detection, the synchronization of the control signals of (Q_{21}-Q_{24}, Q_{31}-Q_{34}) are ensured, enabling the control of the conduction angles (β_2, β_3). Moreover, the values of β_2, β_3 can be adjusted by a PI regulator to achieve a specific output current.

In addition, during the PI progress, the regulated values (β_2, β_3) can be further used to estimate the mutual inductance. Combining (3) and (10), the values of M_{12} and M_{13} can be obtained as

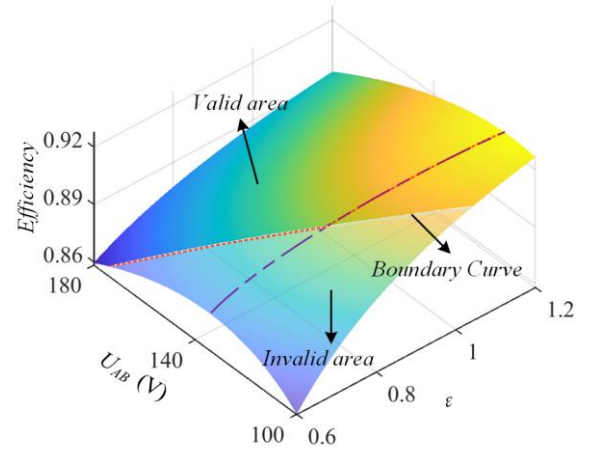Fig 7. The trend surface of the efficiency with U_{AB} and ε (V_3=80V, I_{3DC}=10A, M_{13}=25µH, α=1.1 and γ=1).

$$M_{12} = \frac{\pi\omega L_{f1}L_{f2}I_{2DC}}{2\sqrt{2}U_{AB}\sin(\beta_2)}, M_{13} = \frac{\pi\omega L_{f1}L_{f3}I_{3DC}}{2\sqrt{2}U_{AB}\sin(\beta_3)} \quad (16)$$

B. Transmitter side control for MEPT

Based on the description in Section II, the input voltage U_{AB} needs to be regulated in order to achieve the maximum efficiency point tracking. In this paper, U_{AB} is modulated by phase shift modulation as depicted in Fig.3.

The relationship between the output voltage U_{AB} and the output voltage of the H-bridge, V_1 can be expressed as

$$U_{AB} = \frac{2\sqrt{2}}{\pi}V_1\sin(\beta_1/2) \quad (17)$$

Combining (17) and (15), the optimal conduction angle of the inverter can be given by

$$\beta_{1opt} = 2\arcsin(\frac{\pi U_{AB-opt}}{2\sqrt{2}V_1}) \quad (18)$$

Equation (18) provides the proposed theoretical basis for the MEPT method. During the charging process, when β_1 reaches β_{1opt}, the minimum I_{1DC} is obtained and the individual receiver coil charging current reaches the target value.

However, it is worth noting that U_{AB-opt} is not available in all cases. This is because the coupling at the RX side and the requirement current constrains the minimum input voltage. Combing (3) and (10), the minimum input voltage required for the two RXs ($U_{AB-2min}$, $U_{AB-3min}$) respectively can be obtained as:

$$U_{AB-2min} \geq \frac{\pi\omega L_{f1}L_{f2}I_{2DC-D}}{2\sqrt{2}M_{12}}, U_{AB-3min} \geq \frac{\pi\omega L_{f1}L_{f3}I_{3DC-D}}{2\sqrt{2}M_{13}} \quad (19)$$

Accordingly, the maximum feasible input voltage for maximum efficiency (U_{AB-fme}) can be obtained as shown in the followed:

$$U_{AB-fme} = \max(U_{AB-opt}, U_{AB-2min}, U_{AB-3min}) \quad (20)$$

Further, equation (18) can be rewritten as

$$\beta_{1fme} = 2\arcsin(\frac{\pi U_{AB-fme}}{2\sqrt{2}V_1}) \quad (21)$$

β_{1fme} represents the feasible conduction angle of the inverter to achieve maximum efficiency.

According to (19), it can be observed that when the current demand increases and the mutual inductance decreases, $U_{AB-2/3min}$ tends to exceed U_{AB-opt}. This can be verified in Fig. 7 using the same parameters listed in Table I.

Equation (19) defines which combinations fulfill the required output power. The combination that achieves the required output operation forms the "Valid area", while the combination that does not achieve the required output is defined as the "Invalid area". These two surfaces are divided by a boundary curve, as shown in Fig. 7. Furthermore, the curve of U_{AB-opt} is plotted according to (15) and is defined as "Desirable MEPT curve". Similarly, the curve of U_{AB-fme} is plotted using (20) and is defined as "Feasible MEPT Curve". It can be clearly seen that the U_{AB-fme} of the system changes from U_{AB-opt} to $U_{AB-2/3min}$ when one of the coupling coefficients decreases (i.e., ε decreases).

Based on the above calculation, the MEPT controller is designed and its logic flowchart is portrayed in Fig. 8. Considering the existence of switching losses in the rectifiers and inverter circuits along with the possible deviation of the mutual inductance estimation, the actual value of β_{1fme} may have a small error with the theoretical result. Therefore, the perturbation observation method [43] is used to accurately locate the maximum efficiency point by calculating and comparing the overall system efficiency. The detailed process is described as follows.

Step 1: The initial conduction angle β_1 of the inverter is set to an initial value of 90° and the conduction angle β_2 and β_3 of the rectifiers are set to a maximum value of 180°. The system is excited accordingly and the associated parameters can be further calculated.

Step 2: The system parameters (mutual inductance, load voltage and output current and output current demand) of the transmitter and receiver sides are detected, and the theoretical optimal phase β_{1fme} is calculated by (21).

Step 3: Record β_{1fme} as $\beta_1(0)$ at this point, measure the input DC current I_{1DC} and record it as $I_{1DC}(0)$, meanwhile, set $k = 0$.

Step 4: The duty cycle is adjusted slightly to $\beta_1(k+1) = \beta_1(k)+\Delta\beta_1$, and then the corresponding $I_{1DC}(k+1)$ is measured and recorded.

Step 5: The direction of the maximum efficiency search (increase or decrease $\Delta\beta_1$) depends on the comparison between $I_{1DC}(k)$ and $I_{1DC}(k+1)$. If $I_{1DC}(k+1) < I_{1DC}(k)$, which means that the increase in β_1 is close to the actual β_{1fme}, then β_1 continuously increases $\beta_1(k+1)=\beta_1(k)+\Delta\beta_1$. On the contrary, if $I_{1DC}(k+1) \geqslant I_{1DC}(k)$, which means that the increase in β_1 deviates from β_{1fme}, therefore, β_1 needs to be reduced by applying $\beta_1(k+1)=\beta_1(k)-\Delta\beta_1$.

Step 6: To obtain the optimal efficiency, similarly the comparison is performed with the combination of $I_{1DC}(k)$ and $I_{1DC}(k+1)$. If $I_{1DC}(k+1)$ has been decreasing compared to $I_{1DC}(k)$, it indicates that the increasing or decreasing of β_1 has been improving the system

efficiency and the value of β_1 value is converging to realistic β_{1fme}. If $I_{1DC}(k+1)$ is greater than or equal to $I_{1DC}(k)$, then it can be concluded that the maximum efficiency is reached at this time. Accordingly, $\beta_1(k)$ and $I_{1DC}(k)$ can be considered as β_{1fme} and the I_{1DCmin}.

Step 7: To ensure that the system is always operating at maximum efficiency, $\beta_1(k)$ is used as $\beta_1(0)$ for the next iteration.

IV. EXPERIMENTAL VALIDATION

A. The Prototype Setup

Fig. 9 depicts a 2kW single TX dual RXs laboratory prototype developed to experimentally validate the proposed the MEPT method with the same parameters presented in Table I.

The feasibility of the proposed method under the misalignment between the charging pads is investigated. The resultant variation in mutual inductance caused by the misalignment of the receiving coils is shown in Fig. 9(b). Obviously, the mutual inductance decreases significantly with increasing misalignment. Furthermore, [-70mm, 70mm] is set as the range of lateral misalignment of the receiving coil.

Three DSP28335 controllers are used on both sides to generate the required PWM signals to drive the inverter and controlled rectifiers. Meanwhile, low drain-source on state resistance Sic MOSFETs (C3M0016120D) are utilized for both the inverter and rectifiers. On the receiver side, ITECH electronic loads are used to emulate the battery behavior and system efficiency is measured by YOKOGAWA WT1800.
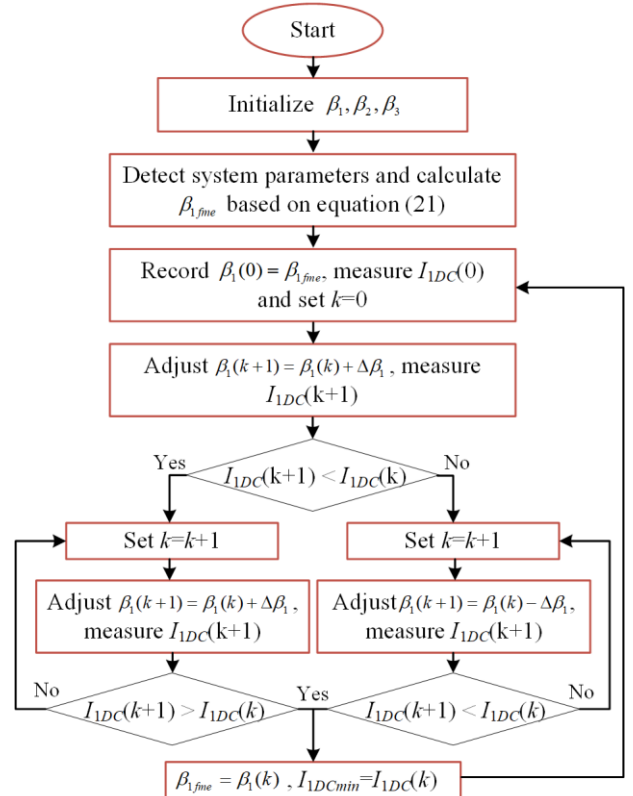

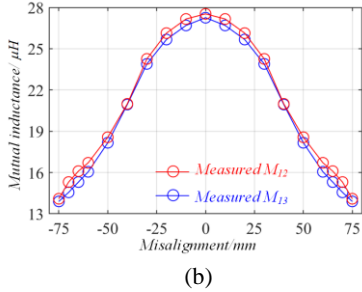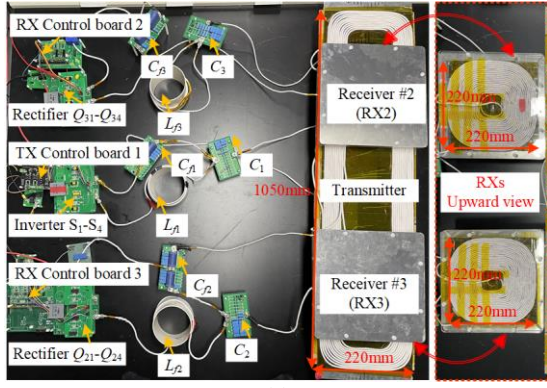Fig 8. Flowchart of the proposed PO-based MEPT method.

(a)

(b)

Fig 9. View of the prototype of the proposed WPT system. (a) Overall view of the prototype. (b) Mutual inductance of the lateral misalignment.
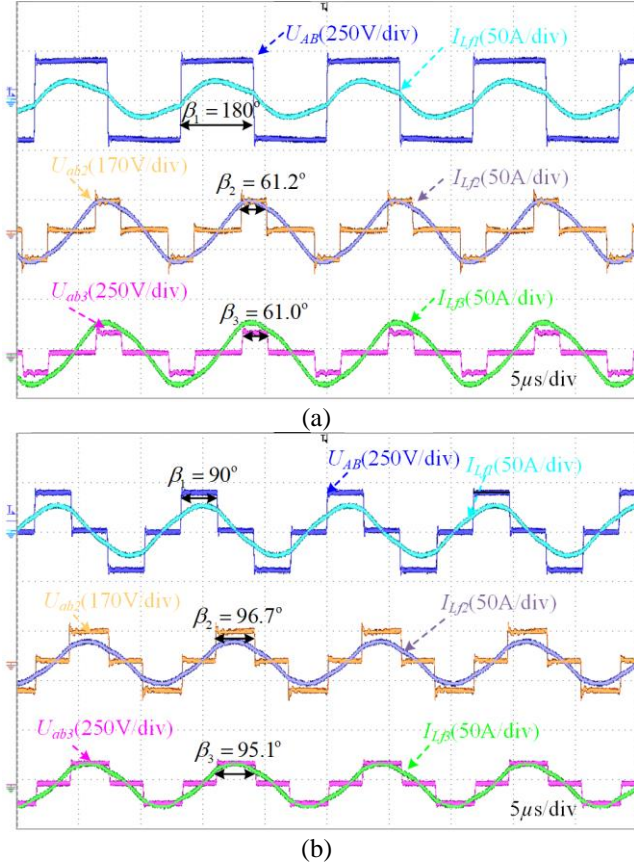
Furthermore, the band-pass filter and phase shift circuit mentioned in [33] are used for zero crossing detection, thus ensuring the accuracy of the synchronization.

B. Experimental waveforms

In order to experimentally demonstrate the effectiveness of the proposed MEPT controller, the input voltage is regulated in the form of adjusting the inverter phase shift angle. Meanwhile, conventional control experiments without the MEPT method are also carried out, where the transmitter input voltage is fixed and specific outputs are achieved by only adjusting the receiver controlled rectifier bridge.

1) Case I: operation under identical loads (i.e. $V_3=V_2=100$V, $I_{3DC}=I_{2DC}=10$A, $M_{13}=M_{12}=27.5\mu$H).

Fig. 10 illustrates a comparative practical key-waveforms of the inverter with different control methods, U_{AB}, I_{Lf1} and I_{L1} at the transmitter side along with U_{ab2}, I_{Lf2}, U_{ab3} and I_{Lf3} at the RX side for both loads of 1kW.

When the system is operating without the MEPT method, it is feasible to make the system achieve a given output by adjusting the β_2, β_3 of the controlled rectifier bridge, as shown in Fig. 10(a). As can be observed, the circuit currents and β_2, β_3 are almost identical for both RXs due to the identical parameter settings. At this point the β_1 of the transmitter side is not adjusted and the measured system efficiency is 85.52%. However, when the MEPT is applied by modifying β_1, the

(a)

(b)

Fig 10. Experiment waveforms of $U_{AB},U_{ab2},U_{ab3},I_{Lf1},I_{Lf2},I_{Lf3}$ in identical load ($V_3=V_2=100$V, $I_{3DC}=I_{2DC}=10$A, $M_{13}=M_{12}=27.5\mu$H).(a) Conventional method without MEPT. (b) Proposed MEPT method.
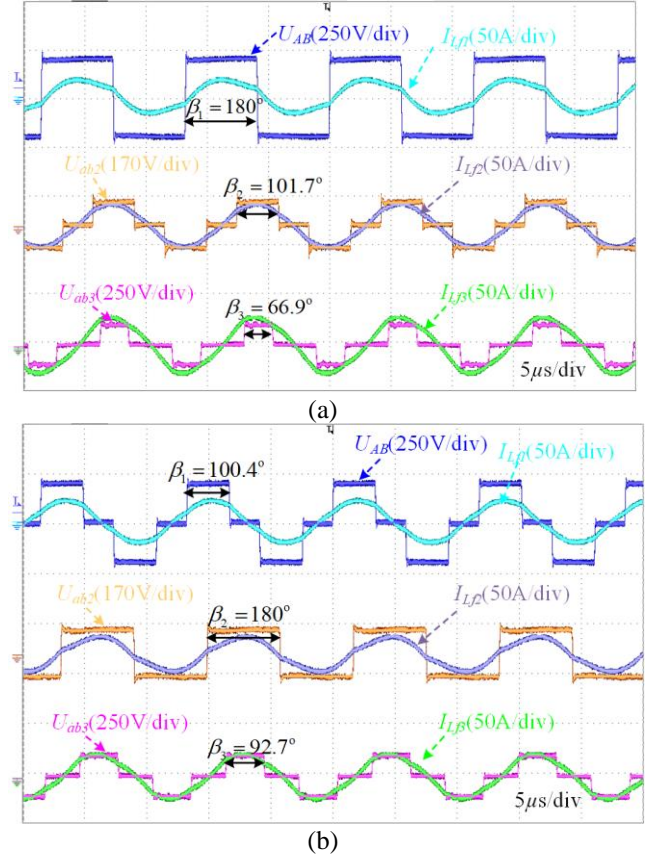

(a)

(b)

Fig 11. Experiment waveforms of $U_{AB},U_{ab2},U_{ab3},I_{Lf1},I_{Lf2},I_{Lf3}$ in differential load ($V_3=100$V, $I_{3DC}=11$A, $M_{13}=24.7\mu$H, $V_2=80$V, $I_{2DC}=8$A, $M_{13}=20.5\mu$H).(a) Conventional method without MEPT. (b) Proposed MEPT method.

optimum efficiency is achieved. As the original β_1 decreases, the corresponding β_2 and β_3 will then increase, which means that the losses caused by I_{L1}, I_{Lf2}, I_{Lf3} will decrease and the losses caused by I_{L2}, I_{L3}, I_{Lf1} will increase. Moreover, when the combined losses reach the lowest value, the maximum efficiency of system is achieved. At this point the actual $U_{AB\text{-}fme}$ = 127.32V, β_1 = 90° and the efficiency is 88.53%, which is a 3% improvement compared to not using MEPT.

2) Case II: operation under unequal loads (i.e. V_3=100V, I_{3DC} =11A, M_{13}=24.7μH, V_2=80V, I_{2DC} =8A, M_{12}=20.5μH).

A similar comparative study is carried out and the key waveforms with and with the proposed method are portrayed in Fig. 11. The differentiated output requirements of both loads are achieved by the individual regulation of the controlled rectifiers on the RX side. Based on (11), in this case, the theoretical $U_{AB\text{-}fme}$=129.4V and $\beta_{1\text{-}fme}$=91.88°. Correspondingly, the measured U_{AB} and β_1 for achieving maximum efficiency are 137.9V and 100° respectively. The difference between the actual and ideal values is mainly due to the switching losses of the semiconductor devices and the magnetic losses of the magnetic couplers, which cause a certain shift in the optimal value. However, interestingly, when
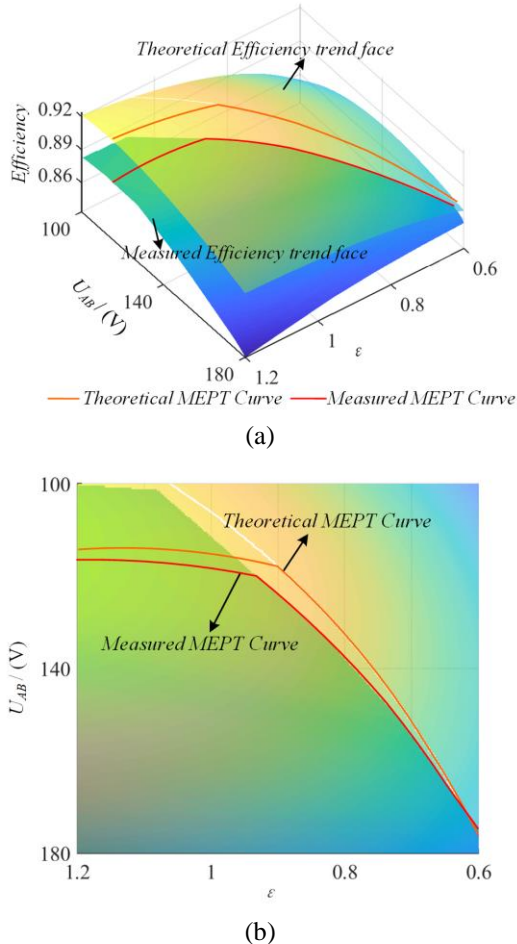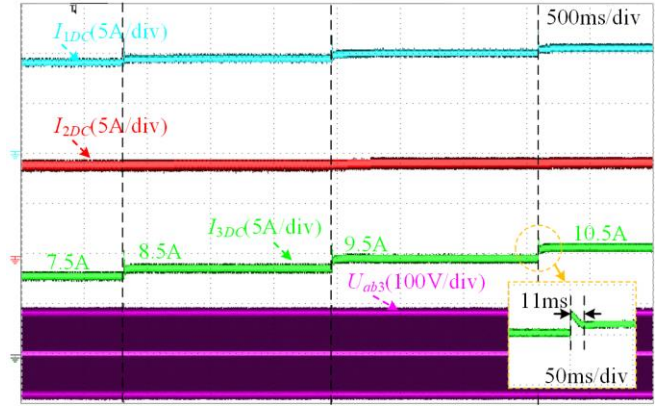

Fig 12. The dynamic response waveforms of proposed method. (V_3=100, I_{3DC}=7.5-10.5A, M_{13}=25μH, V_2=100V, I_{2DC}=9A, M_{12}=25μH)

the proposed MEPT algorithm is applied, the optimal efficiency of 89.13% still can be attained (i.e. 2.8% improvement compared to that without MEPT).

3) Case III: Dynamic performance of the proposed method (V_3=100, I_{3DC}=7.5A-10.5A, M_{13}=25μH, V_2=100V, I_{2DC}=9A, M_{12}=25μH).

The performance of the proposed MEPT is also verified with a step change in load demand current (i.e. from 7.5A to 10.5A) as demonstrated in Fig. 12. It can be seen, the output current on the RX3 can quickly reach the required value without impacting the output current of RX2.

4) Case IV: System efficiency versus different U_{AB} and ε (V_3=80V, I_{3DC}=10A, M_{13}=22.91μH, V_2=88V, I_{2DC}=9A, M_{12}=14-27.5μH, ε=0.6-1.2).

Fig. 13(a) illustrates the variation in efficiency of the proposed IPT system with different U_{AB} and mutual inductance, the theoretical MEPT curve and measured MEPT curve are also plotted. The slightly transparent surface located on the upper side of the image is the theoretical efficiency trend surface, while the surface located on the lower side is the measured efficiency trend surface. The system efficiency varies with the U_{AB} when the M_{12} is fixed while ε is fluctuating, it can be observed that the measured efficiency falls below the theoretical efficiency, the main reason is that the switch losses of inverter, rectifier and magnetic losses of the magnetic

(a)

(b)

Fig 13. The trend surface of the efficiency with U_{AB} and ε (V_3=80V, I_{3DC}=10A, M_{13}=22.91μH, V_2=88V, I_{2DC}=9A, M_{12}=14-27.5μH, ε=0.6-1.2). (a) Three-dimensional view. (b) Projected two-dimensional view
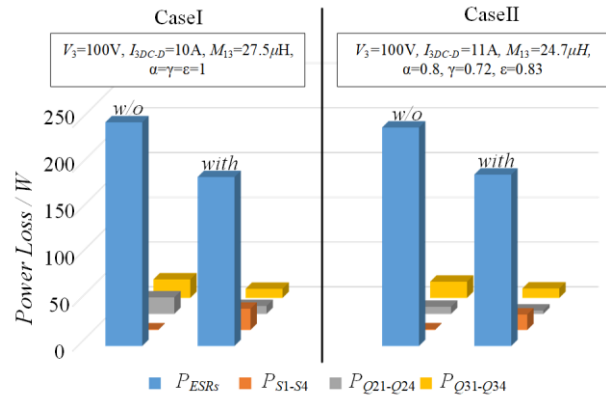

Fig 14. Measured power distribution of the system with and without MEPT at identical loads (Case I) and at differential loads (Case II).

Table II Compreative analysis with previous work

Reference	[27]	[34]	[20]	[21]	[35]	[32]	[39]	This work
Resonant tank	S-S	S-S	S-S	LCC-S	LCC-S	LCC-S	S-LCC	LCC-LCC
Independent RXs	YES	NO	NO	YES	YES	YES	YES	YES
Coupling coefficient	-	0.2-0.3	0.21	0.21	0.12	0.1,0.2,0.3	0.51	0.09-0.18
Complex and tedious calculations	High	Media	Media	Media	Low	Media	Low	Low
Maximum Efficiency optimization	No	No	Yes	Yes	Yes	No	Yes	Yes

couplers are not considered in the proposed method. However, this does not degrade the performance of the system, as the measured and theoretical efficiency trend face have the same tendency. Moreover, the measured MEPT curve with the proposed tracking method is always close to the theoretical MEPT curve in Fig. 13(b). This intuitively proves that the proposed method can effectively track the maximum efficiency of the system regardless of varying load resistance and mutual inductance.

For completeness, the power loss distribution of the system under case I and II are illustrated in Fig. 14 as an example. The P_{ESRs} represent the conduction losses which incorporate the conduction losses in the resonant cavity, inverter and rectifiers. P_{S1-S4}, $P_{Q21-Q24}$, $P_{Q31-Q34}$ represent the switching losses of the inverter, the rectifier bridge of RX2 and the rectifier of RX3 respectively. It is clear that MEPT offers a significant reduction in P_{ESRs}, i.e. 70.6W and 52.6W reduction in Case I and Case II, respectively. As for the part on switching losses of MOSFETs, it can be seen that with the MEPT, the losses of P_{S1-S4} gradually increase, while the losses of $P_{Q21-Q24}$, $P_{Q31-Q34}$ gradually decrease. Overall, the total switching loss variation of the MOSFETs is 2.9W and 4.7W for the Case I and Case II respectively. Compared to the fluctuations in P_{ESRs}, the variation in MOSFETs switching losses is quite small. As a result, the method proposed in this paper can effectively locate the optimum voltage value, despite neglecting the switching losses, and can effectively improve the overall system efficiency.

C. Discussion and Comparison

To clearly demonstrate the advantages of this study, a comparison of the performance between the proposed dual side control scheme with previously published related works is presented. Detailed comparison results are provided in Table II. The advantages of the proposed dual side control scheme are listed below.

(1) The proposed method can simultaneously achieve power distribution between independent RXs and MEPT control regardless of variable coupling coefficient and load resistance, which is superior to the method listed in Table II.

(2) This scheme does not require complex and tedious algebraic calculations to evaluate the optimal efficiency point of the system, which is an improvement compared to the scheme proposed in [20,21,27,32,34].

Moreover, it is worth noting that the proposed system design approach is also useful for IPT systems with three or more RXs. The number of variable parameters in the case of more RXs is high and further consideration of the relationships between the individual variables is required. In addition, the optimum input voltage of the system can also be obtained by simplifying (8).

V. CONCLUSION

A single transmitter to dual receivers IPT system was studied with dual side controllable bridges. The focus is on the power transfer characteristics and efficiency of the system in the presence of load voltage, current and coupling variations. A convex optimization model of the system efficiency versus input AC voltage is developed, subsequently, considering the constraints of power distribution and coupling variations on the input AC voltage, the trajectory of the inverter angle satisfying the optimal efficiency is solved. Furthermore, a perturbation observation method is used to optimize the system efficiency in a way that satisfies the minimization of the input current. The experimental set-up is established, the efficiency of the proposed system has been improved compared to the system without MEPT, which can be increased by 3% to 89.13%. Moreover, the measured trajectory of the system is consistent with the theoretical trajectory, which show the feasibility and effectiveness of the proposed method.

REFECENCES

[1] H. Feng, R. Tavakoli, O. C. Onar, and Z. Pantic, "Advances in High-Power Wireless Charging Systems: Overview and Design Considerations," *IEEE Trans. Transp. Electrific.*, vol. 6, no. 3, pp. 886–919, Sep. 2020, doi: 10.1109/tte.2020.3012543.

[2] X. Tian, K. T. Chau, W. Liu, H. Pang, and C. H. T. Lee, "Maximum Power Tracking for Magnetic Field Editing-Based Omnidirectional Wireless Power Transfer," *IEEE Trans. Power Electron.*, vol. 37, no. 10, pp. 12901–12912, Oct. 2022, doi: 10.1109/TPEL.2022.3178097.

[3] S. Y. Hui, "Planar Wireless Charging Technology for Portable Electronic Products and Qi," *Proc. IEEE*, vol. 101, no. 6, pp. 1290–1301, Jun. 2013, doi: 10.1109/jproc.2013.2246531.

[4] S. Wu, C. Cai, X. Liu, W. Chai, and S. Yang, "Compact and Free-Positioning Omnidirectional Wireless Power Transfer System for Unmanned Aerial Vehicle Charging Applications," *IEEE Trans. Power Electron.*, vol. 37, no. 8, pp. 8790–8794, Aug. 2022, doi: 10.1109/TPEL.2022.3158610.

[5] C. Jiang, K. T. Chau, W. Liu, C. Liu, W. Han, and W. H. Lam, "An *LCC* -Compensated Multiple-Frequency Wireless Motor System," *IEEE Trans. Ind. Inf.*, vol. 15, no. 11, pp. 6023–6034, Nov. 2019, doi: 10.1109/TII.2019.2904798.

[6] W. Liu, K. T. Chau, C. H. T. Lee, C. Jiang, W. Han, and W. H. Lam, "A Wireless Dimmable Lighting System Using Variable-Power Variable-Frequency Control," *IEEE Trans. Ind. Electron.*, vol. 67, no. 10, pp. 8392-8404, Oct. 2020, doi: 10.1109/TIE.2019.2947814.

[7] Siqi Li and C. C. Mi, "Wireless Power Transfer for Electric Vehicle Applications," *IEEE J. Emerg. Sel. Topics Power Electron.*, vol. 3, no. 1, pp. 4–17, Mar. 2015, doi: 10.1109/jestpe.2014.2319453.

[8] T. Kan, T.-D. Nguyen, J. C. White, R. K. Malhan, and C. C. Mi, "A New Integration Method for an Electric Vehicle Wireless Charging System Using LCC Compensation Topology: Analysis and Design," *IEEE Trans. Power Electron.*, vol. 32, no. 2, pp. 1638–1650, Feb. 2017, doi: 10.1109/tpel.2016.2552060.

[9] X. Tian, K. T. Chau, W. Liu, and C. H. T. Lee, "Selective Wireless Power Transfer Using Magnetic Field Editing," *IEEE Trans. Power Electron.*, vol. 36, no. 3, pp. 2710–2719, Mar. 2021, doi: 10.1109/TPEL.2020.3017000.

[10] Z. Zhang, X. Li, H. Pang, H. Komurcugil, Z. Liang, and R. Kennel, "Multiple-Frequency Resonating Compensation for Multichannel Transmission of Wireless Power Transfer," *IEEE Trans. Power Electron.*, vol. 36, no. 5, pp. 5169–5180, May 2021, doi: 10.1109/TPEL.2020.3027916.

[11] Z. Zhang and H. Pang, "Continuously Adjustable Capacitor for Multiple-Pickup Wireless Power Transfer Under Single-Power-Induced Energy Field," *IEEE Trans. Ind. Electron.*, vol. 67, no. 8, pp. 6418–6427, Aug. 2020, doi: 10.1109/TIE.2019.2937056.

[12] Y. Liu, C. Liu, X. Gao and S. Liu, "Design and Control of a Decoupled Multichannel Wireless Power Transfer System Based on Multilevel Inverters," *IEEE Transactions on Power Electronics*, vol. 37, no. 8, pp. 10045-10060, Aug. 2022, doi: 10.1109/TPEL.2022.3159129.

[13] J. Meng, G. Liu, S. Zhao, Y. Zhai, S. Chen and Y. Wang, "Maximum Efficiency Point Calculation For Multiple Electric Vehicles of Wireless Power Transfer System With LCC-LCC Compensation Topology," 2021 5th CAA International Conference on Vehicular Control and Intelligence (CVCI), Tianjin, China, 2021, pp. 1-4, doi: 10.1109/CVCI54083.2021.9661186.

[14] Z. Tan, F. Liu, H. K. Chan, and H. O. Gao, "Transportation systems management considering dynamic wireless charging electric vehicles: Review and prospects," *Transportation Research Part E: Logistics and Transportation Review*, vol. 163, p. 102761, Jul. 2022, doi: 10.1016/j.tre.2022.102761

[15] W. Liu, K. T. Chau, C. C. T. Chow and C. H. T. Lee, "Wireless Energy Trading in Traffic Internet," *IEEE Transactions on Power Electronics*, vol. 37, no. 4, pp. 4831-4841, April 2022, doi: 10.1109/TPEL.2021.3118458.

[16] H. H. Wu, G. A. Covic, J. T. Boys and D. J. Robertson, "A Series-Tuned Inductive-Power-Transfer Pickup With a Controllable AC-Voltage Output," *IEEE Transactions on Power Electronics*, vol. 26, no. 1, pp. 98-109, Jan. 2011, doi: 10.1109/TPEL.2010.2052069

[17] Y. Zhang *et al.*, "Misalignment-Tolerant Dual-Transmitter Electric Vehicle Wireless Charging System with Reconfigurable Topologies," *IEEE Trans. Power Electron.*, pp. 1–1, 2022, doi: 10.1109/TPEL.2022.3160868.

[18] K. Shi, C. Tang, H. Long, X. Lv, Z. Wang, and X. Li, "Power Fluctuation Suppression Method for EV Dynamic Wireless Charging System Based on Integrated Magnetic Coupler," *IEEE Trans. Power Electron.*, vol. 37, no. 1, pp. 1118-1131, Jan. 2022, doi: 10.1109/TPEL.2021.3097504.

[19] Z. Li, J. Li, S. Li, Y. Yu, and J. Yi, "Design and Optimization of Asymmetric and Reverse Series Coil Structure for Obtaining Quasi-constant Mutual Inductance in Dynamic Wireless Charging System for Electric Vehicles," *IEEE Trans. Veh. Technol.*, vol. 71, no. 3, pp. 2560-2572, March 2022, doi: 10.1109/TVT.2021.3138072.

[20] W. Cai, D. Ma, H. Tang, X. Lai, X. Liu, and L. Sun, "Highly Efficient Target Power Control for Two-Receiver Wireless Power Transfer Systems," *Energies*, vol. 11, no. 10, p. 2726, Oct. 2018, doi: 10.3390/en11102726.

[21] T.-S. Lee, S.-J. Huang, and S.-H. Dai, "Contactless Power Transfer for Rail-Guided Vehicles With Power Equalization and Efficiency Improvement Considerations," *IEEE Trans. Ind. Electron.*, vol. 69, no. 4, pp. 3566–3576, Apr. 2022, doi: 10.1109/TIE.2021.3076728.

[22] R. Bosshard, U. Iruretagoyena, and J. W. Kolar, "Comprehensive Evaluation of Rectangular and Double-D Coil Geometry for 50 kW/85 kHz IPT System," *IEEE J. Emerg. Sel. Topics Power Electron.*, vol. 4, no. 4, pp. 1406–1415, Dec. 2016, doi: 10.1109/JESTPE.2016.2600162.

[23] A. U. Ibrahim, W. Zhong, and M. D. Xu, "A 50-kW Three-Channel Wireless Power Transfer System With Low Stray Magnetic Field," *IEEE Trans. Power Electron.*, vol. 36, no. 9, pp. 9941-9954, Sept. 2021, doi: 10.1109/TPEL.2021.3064373..

[24] W. Zhang and C. C. Mi, "Compensation Topologies of High-Power Wireless Power Transfer Systems," *IEEE Trans. Veh. Technol.*, vol. 65, no. 6, pp. 4768–4778, Jun. 2016, doi: 10.1109/tvt.2015.2454292.

[25] Z. Yan, K. Zhang, L. Qiao, Y. Hu, and B. Song, "A Multiload Wireless Power Transfer System With Concentrated Magnetic Field for AUV Cluster System," *IEEE Trans. on Ind. Applicat.*, vol. 58, no. 1, pp. 1307–1314, Jan. 2022, doi: 10.1109/TIA.2021.3102897.

[26] F. Liu, Y. Yang, Z. Ding, X. Chen, and R. M. Kennel, "A Multifrequency Superposition Methodology to Achieve High Efficiency and Targeted Power Distribution for a Multiload MCR WPT System," *IEEE Trans. Power Electron.*, vol. 33, no. 10, pp. 9005–9016, Oct. 2018, doi: 10.1109/TPEL.2017.2784566.

[27] X. Hou, Z. Wang, Y. Su, Z. Liu, and Z. Deng, "A Dual-Frequency Dual-Load Multirelay Magnetic Coupling Wireless Power Transfer System Using Shared Power Channel," *IEEE Trans. Power Electron.*, vol. 37, no. 12, pp. 15717–15727, Dec. 2022, doi: 10.1109/TPEL.2022.3190143.

[28] M. Fu, H. Yin, and C. Ma, "Megahertz Multiple-Receiver Wireless Power Transfer Systems With Power Flow Management and Maximum Efficiency Point Tracking," *IEEE Trans. Microwave Theory Techn.*, vol. 65, no. 11, pp. 4285–4293, Nov. 2017, doi: 10.1109/TMTT.2017.2689747.

[29] C. Qi, S. Huang, X. Chen, and P. Wang, "Multifrequency Modulation to Achieve an Individual and Continuous Power Distribution for Simultaneous MR-WPT System With an Inverter," *IEEE Trans. Power Electron.*, vol. 36, no. 11, pp. 12440–12455, Nov. 2021, doi: 10.1109/TPEL.2021.3081931.

[30] V.-B. Vu, V.-T. Phan, M. Dahidah, and V. Pickert, "Multiple Output Inductive Charger for Electric Vehicles," *IEEE Trans. Power Electron.*, vol. 34, no. 8, pp. 7350–7368, Aug. 2019, doi: 10.1109/TPEL.2018.2882945.

[31] J. Kim, D.-H. Kim, and Y.-J. Park, "Free-Positioning Wireless Power Transfer to Multiple Devices Using a Planar Transmitting Coil and Switchable Impedance Matching Networks," *IEEE Trans. Microwave Theory Techn.*, vol. 64, no. 11, pp. 3714–3722, Nov. 2016, doi: 10.1109/TMTT.2016.2608802.

[32] R. He, P. Zhao, G. Ning, K. Yue, Y. Liu, and M. Fu, "Optimal Driving and Loading Scheme for Multiple-Receiver Inductive Power Transfer," *IEEE Trans. Ind. Electron.*, vol. 69, no. 12, pp. 12665-12675, Dec. 2022, doi: 10.1109/TIE.2021.3134065.

[33] X. Wang, J. Xu, M. Leng, H. Ma, and T. Dragicevic, "Individually Regulated Dual-Output IPT System Based on Current-Mode Switching Cells," *IEEE Trans. Ind. Electron.*, vol. 68, no. 12, pp. 12930-12934, Dec. 2021, doi: 10.1109/TIE.2020.3047067.

[34] X. Wang, J. Xu, S. Lu, S. Ren, M. Leng, and H. Ma, "Single-Receiver Multioutput Inductive Power Transfer System With Independent Regulation and Unity Power Factor," *IEEE Trans. Power Electron.*, vol. 37, no. 1, pp. 1159–1171, Jan. 2022, doi: 10.1109/TPEL.2021.3100055.

[35] L. Zhou *et al.*, "Efficiency Optimization of LCC-S Compensated Multiple-receiver Bi-directional WPT System for Stackers in Automated Storage and Retrieval Systems," *IEEE Trans. Power Electron.*, pp. 1–1, 2022, doi: 10.1109/TPEL.2022.3173954.

[36] Y. Li *et al.*, "Extension of ZVS Region of Series–Series WPT Systems by an Auxiliary Variable Inductor for Improving Efficiency," *IEEE Trans. Power Electron.*, vol. 36, no. 7, pp. 7513–7525, Jul. 2021, doi: 10.1109/tpel.2020.3042011.

[37] R. Mai, Y. Liu, Y. Li, P. Yue, G. Cao, and Z. He, "An Active-Rectifier-Based Maximum Efficiency Tracking Method Using an Additional Measurement Coil for Wireless Power Transfer," *IEEE Trans. Power Electron.*, vol. 33, no. 1, pp. 716–728, Jan. 2018, doi: 10.1109/tpel.2017.2665040.

[38] K. Song *et al.*, "Constant Current Charging and Maximum System Efficiency Tracking for Wireless Charging Systems Employing Dual-Side Control," *IEEE Trans. on Ind. Applicat.*, vol. 56, no. 1, pp. 622-634, Jan.-Feb. 2020, doi: 10.1109/TIA.2019.2942278.

[39] H. Yang *et al.*, "Efficiency Analysis and Optimization Method of Power-Relay IPT Systems for Reefer Containers," *IEEE Trans. Power Electron.*, vol. 36, no. 5, pp. 4942–4947, May 2021, doi: 10.1109/TPEL.2020.3030902.

[40] K. K. Ean, B. T. Chuan, T. Imura and Y. Hori, "Impedance matching and power division algorithm considering cross coupling for wireless power transfer via magnetic resonance," *Intelec 2012*, Scottsdale, AZ, USA, 2012, pp. 1-5, doi: 10.1109/INTLEC.2012.6374468.

[41] M. Fu, H. Yin, M. Liu, Y. Wang, and C. Ma, "A 6.78 MHz Multiple-Receiver Wireless Power Transfer System With Constant Output Voltage and Optimum Efficiency," *IEEE Trans. Power Electron.*, vol.

33, no. 6, pp. 5330–5340, Jun. 2018, doi: 10.1109/TPEL.2017.2726349.

[42]   S. Li, W. Li, J. Deng, T. D. Nguyen, and C. C. Mi, "A Double-Sided LCC Compensation Network and Its Tuning Method for Wireless Power Transfer," *IEEE Trans. Veh. Technol.*, vol. 64, no. 6, pp. 2261–2273, Jun. 2015, doi: 10.1109/tvt.2014.2347006.

[43]   X. Wang, J. Xu, M. Leng, H. Ma, and S. He, "A Hybrid Control Strategy of *LCC* -S Compensated WPT System for Wide Output Voltage and ZVS Range With Minimized Reactive Current," *IEEE Trans. Ind. Electron.*, vol. 68, no. 9, pp. 7908–7920, Sep. 2021, doi: 10.1109/TIE.2020.3013788.